

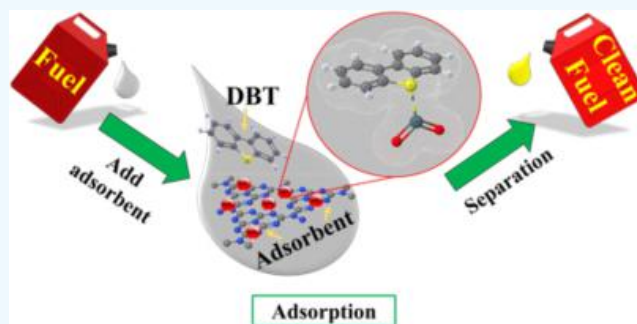
Kinetics of Sulfur Removal from Tehran Vehicular Gasoline by g-C₃N₄/SnO₂ Nanocomposite

Seyed Mohammad Montazeri and Seyed Khatiboleslam Sadrnezhad*[✉]

Department of Materials Science and Engineering, Sharif University of Technology, Azadi Ave., P.O. Box 11155-9466, Tehran 145888-9694, Iran

ABSTRACT: The graphitic carbon nitride/tin oxide (g-C₃N₄/SnO₂) nanocomposite synthesized under microwave irradiation was used for adsorptive removal of sulfur-containing dibenzothiophene (DBT) from Tehran vehicular gasoline. High-resolution transmission electron microscopy, X-ray powder diffraction, energy dispersive X-ray spectroscopy, Brunauer–Emmett–Teller, Fourier-transform infrared spectroscopy, and field emission scanning electron microscopy techniques determined the adsorbent characteristics, and gas chromatography with a flame ionization detector determined the DBT concentration of the samples. Application of the experimental data into the solid/fluid kinetic models indicated

a chemisorption control regime that increased the removal of sulfur from the commercial samples used. A pseudo-second-order reaction with the rate constant of 0.015 (g mg⁻¹ min⁻¹) and total conversion time of 316 min described the adsorption process. Based on the real fuel results, the adsorption capacity of the g-C₃N₄/SnO₂ adsorbent reached 10.64 mg S g⁻¹ adsorbent at equilibrium conditions. This value was the highest adsorption capacity obtained so far for a commercial gasoline sample. The g-C₃N₄/SnO₂ nanocomposite could, therefore, be introduced as an inexpensive, easily obtainable adsorbent that can significantly remove the sulfur from the vehicular gasoline fuels.



INTRODUCTION

Environmental concerns have compelled fuel refineries to remove the sulfur-containing compounds from transportation fuels.^{1,2} Removal of sulfur compounds leads to increase of combustion engine lifetime and positive environmental attitudes. Research on clean fuel has been considered for many years to reduce air pollution and prevent the introduction of pollutants into the environment.^{3,4} Existing sulfur compounds in fuel cause emission of SO_x, which increases the possibility of acid rain.^{4–6} Accordingly, many strict regulations have been established in many countries to reduce sulfur content in public transportation fuels such as diesel and gasoline.⁷ Recent regulations for the reduction of the current sulfur content to less than 10 ppm have been proposed.⁸

Improvement of the fuel cell technology is now a hot issue in research and development units of the industries. Fuel cells consume gasoline and diesel as the direct or indirect primary fuels. Since a solid oxide fuel cell works at high temperatures, the sulfur content should be less than 10 ppm. Furthermore, deep desulfurization below 1 ppm for proton-exchange-membrane fuel cell is also required.^{2,9,10}

Traditional hydrodesulfurization has been used to lower sulfur content as a conventional process.¹¹ This process is complicated and costly especially for the removal of some sulfur compounds like dibenzothiophene (DBT) and its derivatives that are present in a few tens of ppm when a profound desulfurization goal is usually required.^{5,12–14}

Besides, about 90% of the sulfur content of the studied gasoline in this research is in DBT. The removal of these compounds from transportation fuels (primarily diesel and gasoline) has been a controversial topic in the industry.^{15,16} In this regard, alternative or complementary desulfurization processes for ultralow sulfur fuel production have been evolved such as oxidative desulfurization,^{17–20} biodesulfurization,²¹ extraction,^{22–25} and adsorptive desulfurization.^{26–29} Investigations have shown that adsorptive desulfurization is a promising procedure at the ambient temperature and pressure because of its low-energy consumption and investment costs.

Various adsorbents have been studied before. Yang and co-workers used π -complexation-based sorbents that were obtained by ion-exchanging faujasite-type zeolites with Cu⁺, Ni²⁺, or Zn²⁺ cations. They reported Cu(I)-Y (VPIE) as the best sorbent with adsorption capacities of 0.395 and 0.278 (mmol S g⁻¹ sorbent) for commercial jet fuel and diesel, respectively.³⁰ Over past 2 decades, several studies have been conducted on using zeolite,³¹ alumina,²⁷ mesoporous silica,³² and activated carbon³³ as supports for various sorbents to remove sulfur-containing compounds. For instance, Sarda et al. prepared adsorbents by varying the Ni/Cu loadings onto ZSM-5 (Si/Al = 20) and the activated alumina for removal of sulfur from diesel fuel. Their results showed that sulfur removal

Received: May 7, 2019

Accepted: July 24, 2019

Published: August 6, 2019

strongly depends on the nature and amount of the metal and the support material. Their results showed that the activated alumina has a higher sulfur removal power than ZSM-5 due to the more facile diffusion of the large sulfur molecules to the larger pores of the activated alumina than ZSM-5.²⁷

Tin oxide has recently been used in a variety of applications such as gas sensors, dye-based solar cells, optoelectronic devices, electrode materials, and catalysis.³⁴ The presence of active sites on the surface of SnO₂ particles results in a suitable catalytic behavior.³⁵ In a previous study, the authors presented the synthesis and characteristics of the porous graphitic carbon nitride (g-C₃N₄) nanocomposite,³⁶ which seemed usable for the construction of the support substance needed for sulfur removal from the hydrocarbon fuels. According to our knowledge, the g-C₃N₄/SnO₂ nanocomposite has not been used as the adsorbent of sulfur compounds in any studies until now. This study aims to find a high-capacity adsorbent for the removal of sulfur from a highly used commercial petroleum product. Effects of contact time and adsorbent dose on sulfur-containing DBT removal from the regular gasoline of a local Iranian gas station are investigated. Different mathematical correlations are examined to find out the appropriate kinetic model that governs the process. The implication of the devised technique leads to the maximum adsorption capacity of 10.64 mg S g⁻¹ adsorbent, which is obtainable after reaching the equilibrium conditions.

RESULTS AND DISCUSSION

The X-ray powder diffraction (XRD) patterns of the g-C₃N₄/SnO₂ nanocomposite before and after calcination are shown in Figure 1. The design of the calcined powder represents the

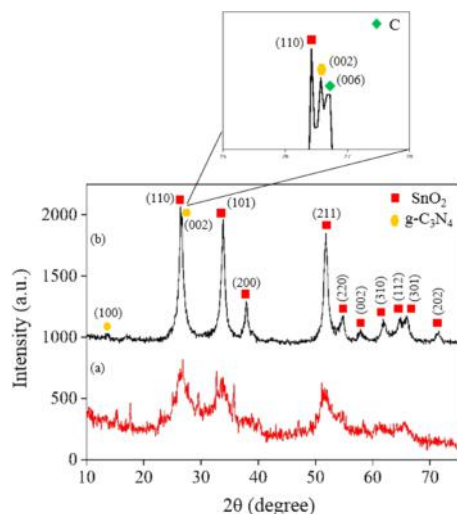


Figure 1. XRD patterns of the g-C₃N₄/SnO₂ nanocomposite (a) before calcination (b) after calcination at 550 °C for 1 h.

significant formation of the tetragonal-phase SnO₂ according to JCPDS card no. 88-0287 with the characteristic peaks located at 2θ angles of 26.50, 33.86, and 51.84°. The magnified portion of the figure indicates the existence of a peak at 26.74°. This peak belongs to the g-C₃N₄ (002) crystallographic plane.³⁷ g-C₃N₄ has another peak at 13.66°, which is also observed in the XRD pattern shown in Figure 1. Overlapping of the characteristic SnO₂ (110) peak with the g-C₃N₄ (002) peak has been the source of confusion in analyzing the XRD patterns of the g-C₃N₄/SnO₂ composites, as reported in the

previous papers.^{36,38} The current study resolved the issue by nanocomposite powder calcination at 550 °C. Based on the JCPDS Card No. 26-1076, the third peak seen in the magnified insets of Figures 1 and 9 attributes to the carbon hexagonal phase. During powder calcination at 550 °C, a meager amount of g-C₃N₄ decomposes to this hardly observable tiny phase, plus evolving gaseous nitrogen. The crystallite average size of different nanocomposite samples was evaluated from the Scherrer equation.³⁹ It was ~14.59 nm before heating and 18.83 nm after calcination, which confirmed particle size growth during calcination.

Field-emission scanning electron microscope (FESEM) and high-resolution transmission electron microscopy (HRTEM) were used to determine the morphology of the g-C₃N₄/SnO₂ nanocomposite. In Figure 2a, the stacked layers of graphitic carbon nitride with a dimension of about 34.12 μm and highlighted pores are observable. The structure of the sample is less porous than the g-C₃N₄/SnO₂ nanocomposite produced in our previous research.³⁶ During irradiation with microwave, some urea molecules decomposed to gaseous products that tended to exit from the graphitic layers of C₃N₄ toward the root to the porous structure.³⁶ Consequently, the lower amount of urea (the precursor for the fabrication of the g-C₃N₄/SnO₂ nanocomposite) could result in fewer porosities produced in this study sample.

Figure 2b shows the SnO₂ nanoparticles scattered on g-C₃N₄ sheets. From image analysis, the average diameter of these particles is ~23.58 nm. Figure 2d displays the HRTEM image of the SnO₂ nanoparticles (the darker area) accumulated on a carbon nitride sheet. An average diameter of ~14 nm was obtained from the image. This value agreed well with the crystallite size obtained from the XRD by the Scherrer equation. Hindering the particle growth together with a hefty gas evolution due to urea decomposition caused the decrease in average size to ~14 nm. The lattice fingers of the sample are illustrated in Figure 2e. The lattice distance measured is ~0.26 nm, which is indexed as the (101) plane of the SnO₂ as depicted in the XRD pattern in Figure 1.

Figure 3 shows the elemental maps, the energy dispersive X-ray spectroscopy (EDS) spectrum, and the analysis of the g-C₃N₄/SnO₂ nanocomposite produced in this research. According to the maps, all elements (carbon, nitrogen, tin, and oxygen) are uniformly distributed in the sample. The overlap of the elemental maps supports a well-coupled SnO₂ structure on the g-C₃N₄ layers.⁴⁰ The atomic ratio of the Sn–O in the studied area of Figure 3b is not far from 1:2 of a stable SnO₂ molecule. The ratio higher than 3:4 for carbon/nitrogen is due to the decomposition of the stray hydrocarbon complexes that may have contaminated the production chamber.

Figure 4a illustrates nitrogen adsorption/desorption for the g-C₃N₄/SnO₂. The shape of the curves and hysteresis loop suggests type IV isotherms for the sample, which indicates the existence of mesopores.⁴¹ The Brunauer–Emmett–Teller (BET) surface area of the sample was calculated to be 66.36 m² g⁻¹. Figure 4b shows the pore size distributions of the g-C₃N₄/SnO₂ via the BJH (Barrett–Joyner–Halenda) model. Accordingly, the BJH pore volume and the mean pore diameter were measured to be 0.43 cm³ g⁻¹ and 18.76 nm, respectively.

Figure 5 illustrates the effect of contact time on the local gasoline DBT adsorption at 298 K. The original DBT content of the gasoline was 358.51 mg DBT L⁻¹ (62.38 mg S L⁻¹), and

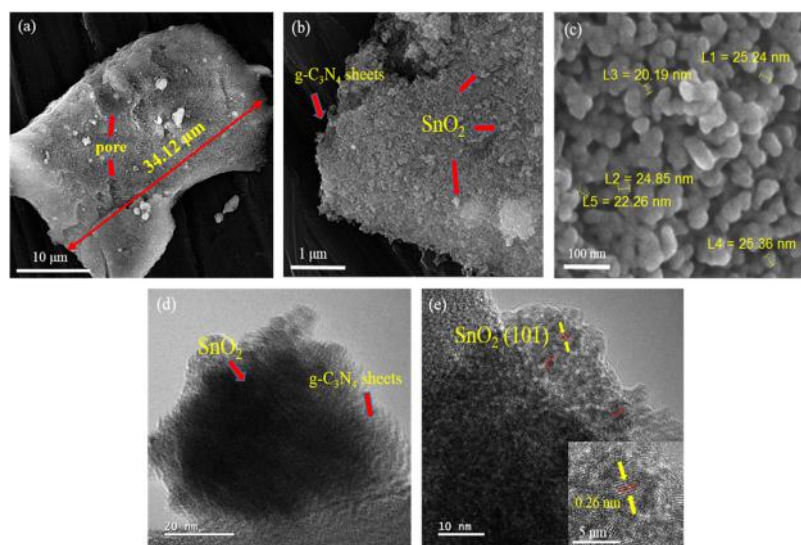


Figure 2. FESEM (a–c) and HRTEM images (d, e) of the $g\text{-C}_3\text{N}_4/\text{SnO}_2$ nanocomposite: (a) graphitic carbon nitride sheet, (b) SnO_2 nanoparticles scattered on the $g\text{-C}_3\text{N}_4$ sheets, (c) SnO_2 nanoparticles' shape and size, (d) SnO_2 nanoparticles accumulated on the $g\text{-C}_3\text{N}_4$ sheets, and (e) lattice fingers of the SnO_2 nanoparticles.

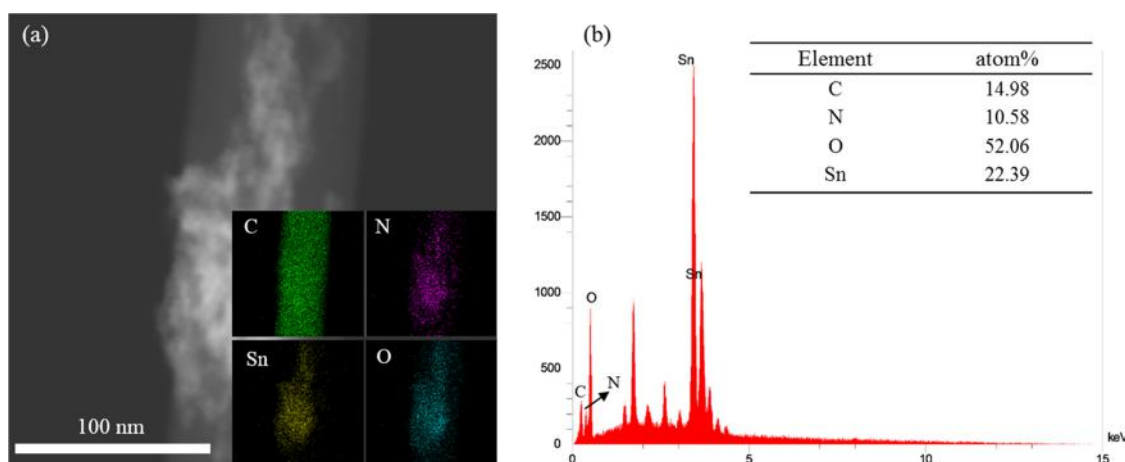


Figure 3. (a) Elemental maps of C, N, Sn, and O in the $g\text{-C}_3\text{N}_4/\text{SnO}_2$ and (b) EDS spectrum of the nanocomposite sample showing the content of the elements present in the $g\text{-C}_3\text{N}_4/\text{SnO}_2$ produced in this research.

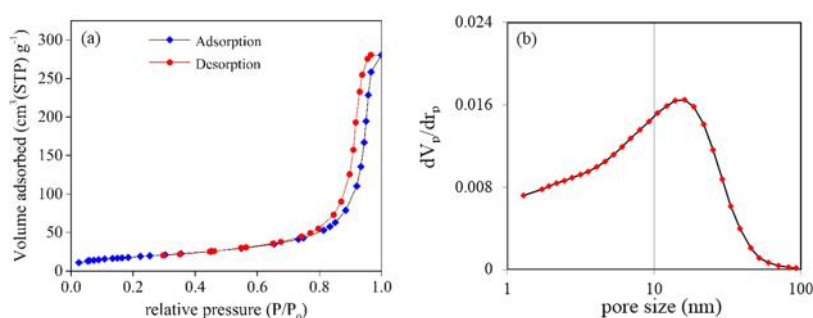


Figure 4. (a) N_2 adsorption/desorption and (b) pore size distributions curves of the $g\text{-C}_3\text{N}_4/\text{SnO}_2$.

its final content after full adsorption was $168.89 \text{ mg DBT L}^{-1}$ ($28.68 \text{ mg S L}^{-1}$). Figure 5 indicates that fast initial adsorption is followed by a slow-down rate that tends to reach the equilibrium state after 180 min. The equilibrium amount is, therefore, $\sim 3.37 \text{ mg S g}^{-1}$ adsorbent. This change is due to the reduction of the active adsorbent sites by adsorbing sulfur atoms.

Effect of Adsorbent Dose on Sulfur Removal. Different doses of the adsorbent were added to each sample at 298 K to remove sulfur from gasoline of the local gas station. The data obtained after stirring the mixture for 360 min were plotted against the adsorbent weight (see Figure 6). The best-fit curve plotted in Figure 6 was used to determine the equilibrium data tabulated in Table 1. These data showed that the sulfur

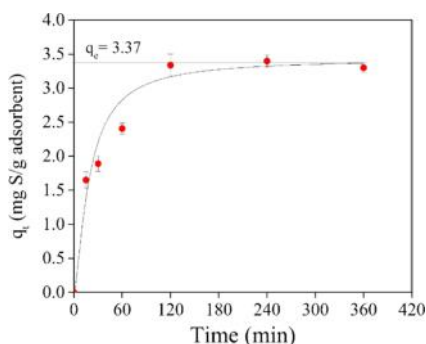


Figure 5. Effect of contact time on S removal from gasoline by $g\text{-C}_3\text{N}_4/\text{SnO}_2$ (adsorbent mass = 0.1 g; $T = 25\text{ }^\circ\text{C}$).

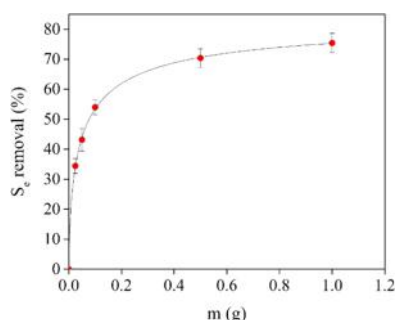


Figure 6. Effect of the adsorbent dose on the removal of the sulfur ($V = 10\text{ mL}$, $T = 25\text{ }^\circ\text{C}$).

Table 1. Equilibrium Data of Sulfur Removal by the $g\text{-C}_3\text{N}_4/\text{SnO}_2$

adsorbent mass (g)	C_e (mg S L^{-1})	S_e removal (%)	q_e (mg g^{-1})
0.025	40.88	34.46	8.60
0.05	35.46	43.16	5.38
0.1	28.68	54.02	3.37
0.5	18.47	70.39	0.88
1	15.31	75.45	0.47

removal tends to 75.45% of the initial value by an adsorbent amount approaching to 1 g in weight. This increase indicated more favorable adsorption conditions with a higher number of particles of larger specific surface areas.

The gas chromatography with a flame ionization detector (GC-FID) chromatogram peaks of the DBT compound obtained from the initial and the desulfurized gasoline samples are compared in Figure 7. The noticeable decline of the areas under the curves by the adsorbent amount represents the rising of desulfurization by the adsorbent amount. This rising trend supports the data plotted in Figure 6.

Adsorption Isotherms. Removal of sulfur was due to the adsorption of DBT by $g\text{-C}_3\text{N}_4/\text{SnO}_2$ that was modeled by two sorption isotherms, Freundlich and Dubinin–Radushkevitch. The characteristic parameters of the models were evaluated from the slope and the intercept of the plots using regression analysis. The linear form of the Freundlich isotherm is as follows⁴²

$$\log q_e = \log k_f + \frac{1}{n} \log C_e \quad (1)$$

where q_e is the removed amount of sulfur after stirring the mixture for 360 min (mg S g^{-1} adsorbent), C_e is the equilibrium sulfur concentration (mg S L^{-1}), and k_f [in $(\text{mg}^{-1/n} \text{L}^{1/n})$]

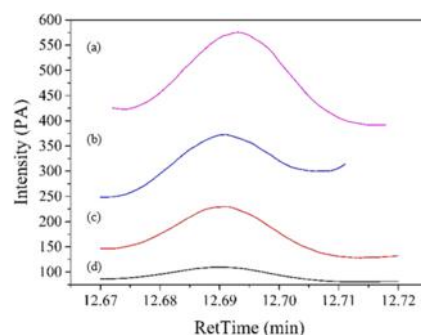


Figure 7. Peaks of DBT obtained from the GC-FID chromatogram for (a) initial gasoline and (b) gasoline treated with 0.1 g, (c) 0.5 g, and (d) 1 g of adsorbent ($V = 10\text{ mL}$; $T = 25\text{ }^\circ\text{C}$).

and n are the Freundlich constants representing the adsorption capacity and rate, respectively.⁴³

The linear form of the Dubinin–Radushkevitch ($D\text{-}R$) isotherm is as follows⁴³

$$\ln q_e = \ln q_m - \beta \varepsilon^2 \quad (2)$$

where q_m (mg g^{-1}) is the theoretical saturation capacity, β ($\text{mol}^2 \text{J}^{-2}$) is the constant related to the mean free energy of adsorption, and ε is the Polanyi potential that is equal to⁴⁴

$$\varepsilon = RT \ln \left(1 + \frac{1}{C_e} \right) \quad (3)$$

In this equation, R ($\text{J mol}^{-1} \text{K}^{-1}$) and T (K) are the ideal gas constant and the absolute temperature, respectively. The adsorption average free energy (E , J mol^{-1}) is related to the change of free energy when 1 mole of the adsorbate transfers from infinity to the surface of the adsorbent in the solution. E can be evaluated from constant β using the following relationship⁴⁵

$$E = \frac{1}{\sqrt{2\beta}} \quad (4)$$

The Freundlich constants k_f and n were evaluated from the data plotted in Figure 8a and are summarized in Table 2. The values of β and q_m of the $D\text{-}R$ isotherm were also obtained from Figure 8b and are tabulated in Table 2. As can be seen in Figure 8 and also in Table 2, the experimental data for removal of sulfur by $g\text{-C}_3\text{N}_4/\text{SnO}_2$ fits better with the Freundlich isotherm ($R^2 = 0.997$) than with the $D\text{-}R$ isotherm ($R^2 = 0.973$). The reason for better fitting of the former is the heterogeneous surface bindings assumed in the Freundlich isotherm.⁴⁶ The low value of E (60.86 J mol^{-1}) indicates that the physical adsorption dominates the system.^{43,45} As a result, the main factor contributing in the mechanism of adsorption is van der Waals interaction forces between adsorbates and adsorbents.⁴³

In this study, the maximum adsorption capacity of $g\text{-C}_3\text{N}_4/\text{SnO}_2$ was obtained to be 8.60 mg S g^{-1} adsorbent, which is 80.83% of the theoretical saturation capacity generated from the $D\text{-}R$ isotherm model. The desulfurization value obtained in this research for the local commercial gasoline, which contained diverse aromatic hydrocarbons, was the highest amount achieved so far. Previous researchers had obtained a relatively low value of 3.5 mg S g^{-1} by graphenelike boron nitride,²⁶ 2.18 mg S g^{-1} by the $\text{Ni}/\text{SiO}_2\text{-Al}_2\text{O}_3$ adsorbent and 1.57 mg S g^{-1} by activated alumina,⁴⁷ 0.32 mg S g^{-1} by zeolite

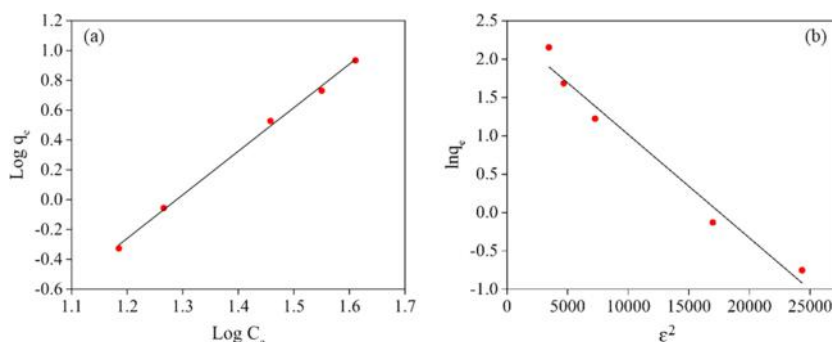


Figure 8. (a) Freundlich and (b) Dubinin–Radushkevitch adsorption isotherms for the removal of sulfur by $g\text{-C}_3\text{N}_4/\text{SnO}_2$.

Table 2. Two Sets of the Isotherm Constants Related to Sulfur Adsorption on the $g\text{-C}_3\text{N}_4/\text{SnO}_2$ Nanocomposite Produced in This Research

model	Freundlich			Dubinin–Radushkevitch				
	parameter	k_f (mg g^{-1}) ($\text{mg}^{-1} \text{L}$) $^{1/n}$	n	R^2	β ($\text{mol}^2 \text{J}^{-2}$)	q_m (mg g^{-1})	E (J mol^{-1})	R^2
$g\text{-C}_3\text{N}_4/\text{SnO}_2$		1.72×10^{-4}	0.343	0.997	1.35×10^{-4}	10.64	60.86	0.973

as an adsorbent,²⁷ 1.2 mg S g^{-1} by 15% $\text{TiO}_2/\text{C-SiO}_2$,⁴⁸ and 7.3 mg S g^{-1} by utilization of 55 wt % metallic Ni with silica–alumina as support of the adsorbent.⁴⁹ The authors focused on the removal of sulfur from the DBT because it was the highest sulfur-containing compound of the selected gasoline.

Removal Mechanism. The XRD pattern of the adsorbent after adsorption was surveyed to confirm the adsorption of DBT on the $g\text{-C}_3\text{N}_4/\text{SnO}_2$. As shown in Figure 9, all of the

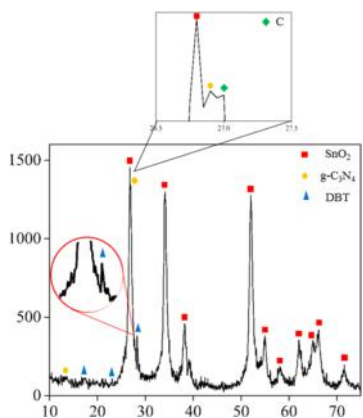


Figure 9. XRD pattern of the adsorbent after the adsorption test.

characteristic peaks of the SnO_2 can be seen according to JCPDS card no. 88-0287. Also, the characteristic $g\text{-C}_3\text{N}_4$ peaks were located at 2θ angles of 27.04 and 13.54°. Therefore, the results indicate that the adsorbent has been stable after the adsorption test. Besides, the peaks at 2θ angles of 28.06, 23.19, and 17.40° belong to the DBT compound according to JCPDS card no. 34-1687.

The Fourier-transform infrared spectroscopy (FTIR) pattern was studied to characterize the structure of the adsorbent ($g\text{-C}_3\text{N}_4/\text{SnO}_2$) before and after the adsorption test. As depicted in Figure 10a, the infra red (IR) peak at around 603.87 cm^{-1} corresponds to the Sn–O stretching vibration, which is related to the characteristic peak of SnO_2 . The peaks at 1403, 1630, and 1722 cm^{-1} are attributed to the stretching mode of C–N heterocycles. The peaks at 806 and 1047 cm^{-1} could be ascribed to the tri-*s*-triazine ring.^{36,50} All of the reported IR

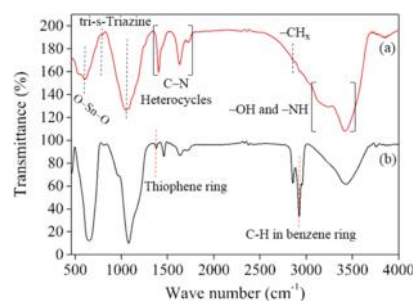


Figure 10. FTIR spectrum of (a) initial adsorbent and (b) utilized adsorbent.

peaks from 806 to 1722 cm^{-1} are characteristic of $g\text{-C}_3\text{N}_4$. Also, the peaks at 2858 cm^{-1} and in the region from 300 to 3500 cm^{-1} are attributed to the stretching vibrations of $-\text{CH}_x$ groups, the N–H bond, and the surface-adsorbed OH groups. These results demonstrate the synthesized adsorbent in which the $g\text{-C}_3\text{N}_4/\text{SnO}_2$ nanocomposite contains both $g\text{-C}_3\text{N}_4$ and SnO_2 . According to Figure 10b, the characteristic peaks of the $g\text{-C}_3\text{N}_4/\text{SnO}_2$ still can be seen in the FTIR spectrum of the utilized adsorbent that represents the stability of the adsorbent after the adsorption test. Besides, the main peaks corresponding to DBT could be distinguished. The bands at 1376 and 2924 cm^{-1} could be allocated to the thiophene ring and C–H in the benzene ring.⁵¹ Also, the band at 1376 cm^{-1} along with the weak band at 1413 cm^{-1} suggests that thiophene coordinates via its sulfur atom to unoccupied metal sites (Sn),⁵² as depicted in Figure 11. Some mechanisms involving π -complexation, which is the formation of bonds between a pair of electrons of sulfur and thin empty s-orbitals, could occur in addition to van der Waals interactions. While for $g\text{-C}_3\text{N}_4$, the most DBT adsorption can probably rely on the physical adsorption of pore channels.

Table 3 illustrates the variation of the sulfur concentration against time. Fractional conversion is evaluated from the following correlation

$$X = \frac{q_t}{q_e} \quad (5)$$

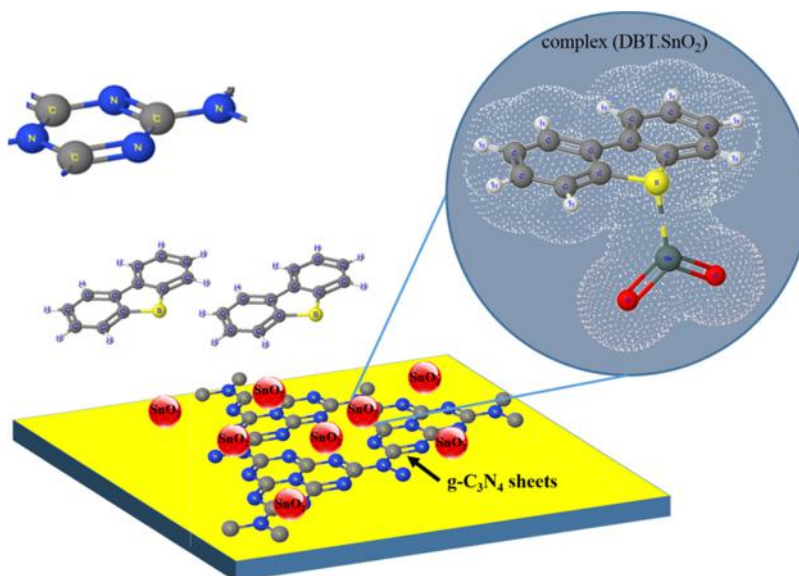


Figure 11. Schematic representation of the sulfur chemisorption mechanism by the $g\text{-C}_3\text{N}_4/\text{SnO}_2$ nanocomposite.

Table 3. Kinetic Data of Sulfur Adsorption on 0.1 g of $g\text{-C}_3\text{N}_4/\text{SnO}_2$

time (min)	C_t (mg S L^{-1})	q_t (mg g^{-1})	X
0	62.38	0	0
15	48.58	1.38	0.41
30	40.28	2.21	0.66
60	34.08	2.83	0.84
120	30.68	3.17	0.94
240	29.18	3.32	0.98
360	28.68	3.37	1

Heterogeneous models for two-phase reactions can be examined with the experimental data for an explanation of the process. The model assumed two steps comprising of mass transfer from gasoline (ext) and adsorption reaction at the gasoline/nanocomposite interface (ads). According to the additive stage times concept and considering the necessary corrections for external mass transfer, the time (t) to achieve a certain degree of conversion (X) can be found as follows.⁵³

$$t = \tau_{\text{ext}} \times q_{f_g}(X) + \tau_{\text{ads}} \times g_{f_g}(X) \quad (6)$$

where t is the overall adsorption time, τ_{ext} and τ_{ads} are time constants for external mass transfer and chemisorption of DBT, respectively, and $q_{f_g}(X)$ and $g_{f_g}(X)$ are mathematical functions describing individual conversion steps for spherical nanoparticles⁵³

$$q_{f_g}(X) = X \quad (7)$$

$$g_{f_g}(X) = 1 - (1 - X)^{1/3} \quad (8)$$

All other combinations, including flat and cylindrical shapes and mixed kinetic regimes, were mathematically examined but did not show closer match with the experimental data. Best-fit examination indicated a total conversion time of $\tau_{\text{ads}} = 316$ min with the possible chemisorption mechanism illustrated in Figure 11.

Pseudo-first and pseudo-second-order rate equations were also tested for best-fit determination^{54,55}

$$\ln(q_e - q_t) = \ln q_e - k_1 t \quad (9)$$

$$\frac{t}{q_t} = \frac{1}{k_2 q_e^2} + \frac{t}{q_e} \quad (10)$$

where k_1 (min^{-1}) and k_2 ($\text{g mg}^{-1} \text{min}^{-1}$) are the pseudo-first and second-order rate constants, respectively. Variations of the left-hand terms of eqs 9 and 10 were plotted against time. From the plots, the rate constants and the coefficients of determination were obtained by the regression analysis evaluation (Figure 12). The results are listed in Table 4. The

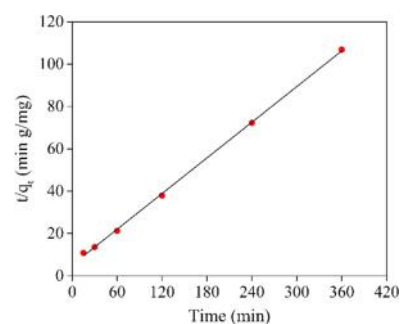


Figure 12. Pseudo-second order verification of the experimental data for sulfur removal from gasoline by $g\text{-C}_3\text{N}_4/\text{SnO}_2$ (adsorbent mass = 0.1 g; $T = 25$ °C).

pseudo-first-order model did not show a straight line for $\ln(q_e - q_t)$ vs t , while the best-fit result belonged to the pseudo-second-order model (Figure 12). The adsorption capacity gained from this model was 3.56 (mg g^{-1}), which was close to the value of 3.37 (mg g^{-1}) obtained from Figure 5. Thus, it was concluded that pseudo-second-order surface adsorption controls the rate of sulfur removal by $g\text{-C}_3\text{N}_4/\text{SnO}_2$.

CONCLUSIONS

The previously introduced $g\text{-C}_3\text{N}_4/\text{SnO}_2$ nanocomposite having the BET surface area of 66.36 ($\text{m}^2 \text{g}^{-1}$) was used as a new sorbent for sulfur removal from the commercial gasoline samples obtained from a domestic gas station in Tehran. The

Table 4. Kinetic Parameters Obtained for Sulfur Removal from Gasoline Based on First- and Second-Order Adsorption Reaction Assumptions

model	pseudo-first-order			pseudo-second-order		
parameter	q_e (mg g ⁻¹)	k_1 (min ⁻¹)	R^2	q_e (mg g ⁻¹)	k_2 (g mg ⁻¹ min ⁻¹)	R^2
value	2.19	0.017	0.952	3.56	0.015	0.999

experimental results showed the increase in sulfur removal with the adsorbent dose, consistent with the well-known Freundlich isotherm equation. Kinetic model calculations showed a single-step mechanism consisting of a pseudo-second-order chemical reaction with the rate constant of 0.015 g mg⁻¹ min⁻¹, which explained the chemisorption of sulfur on the g-C₃N₄/SnO₂ nanocomposite sample. The nanocomposite loaded with the sulfur was then removed by high-speed centrifugation. Due to both ease in production and environmentally friendly process, the g-C₃N₄/SnO₂ nanocomposite was therefore found to be a desirable and promising material for petroleum sulfur elimination applications.

■ EXPERIMENTAL METHODS

Preparation of the Adsorbent. Urea (Merck) as the precursor of carbon nitride, 37% analytical-grade hydrochloric acid (HCl) (density of 1.19 g cm⁻³), and 25% ammonium hydroxide were all obtained from Merck. Commercially available pure tin, ethanol, and deionized (DI) water were purchased from a local chemical supplier. The g-C₃N₄/SnO₂ nanocomposite was synthesized following the procedure described in a previous paper.³⁶ Microwave and urea were used to save energy and reduce the adsorbent cost.

It took 3 h to mix and dissolve 0.175 g of tin in 10 mL of hydrochloric acid. The pH of the solution was adjusted to 12 by adding 300 mL of ammonium hydroxide. One gram of urea was added, and the beaker was placed in a microwave oven operated at 2.45 GHz and 630 W for 30 min. The product was then washed with DI water and ethanol and centrifuged for 5 min at 4000 rpm. The product was dried at 180 °C for 48 h and calcined at 550 °C for 1 h.

Characterization. X-ray diffraction (XRD) patterns of the adsorbents were recorded using a Philips X'Pert Pro MPD with a Cu K α radiation source. The BET surface areas of the adsorbents were measured by the Brunauer–Emmett–Teller (BET) method (BELSORP MINI II) through N₂ adsorption/desorption. The Fourier transform infrared (FTIR) spectra of the samples were recorded on AVATAR (Thermo). The morphology of the adsorbents was investigated by using a field-emission scanning electron microscope (FESEM, Tescan Mira 3-XMU). High-resolution transmission electron microscopy (HRTEM) was performed using a JEM-2100F device equipped with a Gatan Orius SC1000 CCD camera, and the accelerating voltage was 80 kV. The sample powder was ultrasonically dispersed in acetone for approximately 10 min, and the suspensions were deposited on a carbon-coated copper grid. EDS mapping and EDS spectrum were carried out in scanning TEM mode using an Oxford XMax-80T EDS detector and the mentioned FESEM equipped with a SAMX EDS detector, respectively.

Adsorption Process. Gasoline used in the present study was obtained from a local petrol pump, and its total sulfur was determined by a HORIBA SLFA-2800 X-ray fluorescence analyzer (71.6 mg S L⁻¹). Gasoline contained 358.51 mg DBT L⁻¹ sulfur-containing DBT (62.38 mg S L⁻¹). Different amounts of adsorbent's dosage (0.025–1 g) were mixed with

10 mL of gasoline in a shaker for 15–360 min at ambient conditions. Gas chromatography with a flame ionization detector (GC-FID, Agilent 7890A GC) equipped with a DB-5 column ($L = 30$ m; $id = 0.25$ mm) was utilized for detecting the remaining sulfur concentration in the gasoline. The amount of sulfur compound adsorbed onto the sorbent (q_t , mg g⁻¹) is calculated from

$$q_t = \frac{(C_0 - C_t)V}{m} \quad (11)$$

where C_0 and C_t (mg L⁻¹) are sulfur concentrations at the beginning and at time t , respectively, V (L) is the volume of the gasoline, and m (g) is the mass of the adsorbent. The removal percentage of the sulfur can be obtained from

$$S_{\text{removal}}(\%) = \frac{(C_0 - C_t)}{C_0} \times 100 \quad (12)$$

After adsorption, the nanocomposite material containing sulfur species was eliminated from the purified gasoline by centrifugation for 10 min at 6000 rpm.

■ AUTHOR INFORMATION

Corresponding Author

*E-mail: sadrnezh@sharif.edu.

ORCID

Seyed Khatiboleslam Sadrnezhad: 0000-0003-2631-5863

Notes

The authors declare no competing financial interest.

■ ACKNOWLEDGMENTS

General support of the Iran National Science Foundation is gratefully acknowledged.

■ REFERENCES

- (1) Song, C.; Ma, X. New design approaches to ultra-clean diesel fuels by deep desulfurization and deep dearomatization. *Appl. Catal., B* **2003**, *41*, 207–238.
- (2) Bazyari, A.; Khodadadi, A. A.; Haghghat Mamaghani, A.; Beheshtian, J.; Thompson, L. T.; Mortazavi, Y. Microporous titania-silica nanocomposite catalyst-adsorbent for ultra-deep oxidative desulfurization. *Appl. Catal., B* **2016**, *180*, 65–77.
- (3) Ullah, R.; Bai, P.; Wu, P.; Etim, U. J.; Zhang, Z.; Han, D.; Subhan, F.; Ullah, S.; Rood, M. J.; Yan, Z. Superior performance of freeze-dried Ni/ZnO-Al₂O₃ adsorbent in the ultra-deep desulfurization of high sulfur model gasoline. *Fuel Process. Technol.* **2017**, *156*, 505–514.
- (4) Sadrnezhad, S. K. Sulfur Species in Particulates Emitted from Reducing Coal Combustion and Pyrometallurgical Furnaces. *Int. J. Eng.* **1988**, *1*, 73–78.
- (5) Gupta, M.; He, J.; Nguyen, T.; Petzold, F.; Fonseca, D.; Jasinski, J. B.; Sunkara, M. K. Nanowire catalysts for ultra-deep hydrodesulfurization and aromatic hydrogenation. *Appl. Catal., B* **2016**, *180*, 246–254.
- (6) Chandra Srivastava, V. An evaluation of desulfurization technologies for sulfur removal from liquid fuels. *RSC Adv.* **2012**, *2*, 759–783.

- (7) Shu, C.; Sun, T.; Guo, Q.; Jia, J.; Lou, Z. Desulfurization of diesel fuel with nickel boride in situ generated in an ionic liquid. *Green Chem.* **2014**, *16*, 3881–3889.
- (8) Khan, N. A.; Jhung, S. H. Scandium-Triflate/Metal-Organic Frameworks: Remarkable Adsorbents for Desulfurization and Denitrogenation. *Inorg. Chem.* **2015**, *54*, 11498–11504.
- (9) van Rheinberg, O.; Lucka, K.; Köhne, H.; Schade, T.; Andersson, J. T. Selective removal of sulphur in liquid fuels for fuel cell applications. *Fuel* **2008**, *87*, 2988–2996.
- (10) Mahato, N.; Banerjee, A.; Gupta, A.; Omar, S.; Balani, K. Progress in material selection for solid oxide fuel cell technology: A review. *Prog. Mater. Sci.* **2015**, *72*, 141–337.
- (11) Gao, Y.; Han, W.; Long, X.; Nie, H.; Li, D. Preparation of hydrodesulfurization catalysts using MoS₃ nanoparticles as a precursor. *Appl. Catal., B* **2018**, *224*, 330–340.
- (12) Whitehurst, D. D.; Farag, H.; Nagamatsu, T.; Sakanishi, K.; Mochida, I. Assessment of limitations and potentials for improvement in deep desulfurization through detailed kinetic analysis of mechanistic pathways. *Catal. Today* **1998**, *45*, 299–305.
- (13) Ding, W.; Zhu, W.; Xiong, J.; Yang, L.; Wei, A.; Zhang, M.; Li, H. Novel heterogeneous iron-based redox ionic liquid supported on SBA-15 for deep oxidative desulfurization of fuels. *Chem. Eng. J.* **2015**, *266*, 213–221.
- (14) Kwak, C.; Joon, J.; Sang, J.; Choi, K.; Heup, S. Hydrodesulfurization of DBT, 4-MDBT, and 4, 6-DMDBT on fluorinated CoMoS/Al₂O₃ catalysts. *Appl. Catal., A* **2000**, *200*, 233–242.
- (15) Ho, T. C. Deep HDS of diesel fuel: Chemistry and catalysis. *Catal. Today* **2004**, *98*, 3–18.
- (16) Bej, S. K.; Maity, S. K.; Turaga, U. T. Search for an Efficient 4,6-DMDBT Hydrodesulfurization Catalyst: A Review of Recent Studies. *Energy Fuels* **2004**, *18*, 1227–1237.
- (17) Wei, S.; He, H.; Cheng, Y.; Yang, C.; Zeng, G.; Kang, L.; Qian, H.; Zhu, C. Preparation, characterization, and catalytic performances of cobalt catalysts supported on KIT-6 silicas in oxidative desulfurization of dibenzothiophene. *Fuel* **2017**, *200*, 11–21.
- (18) Chen, K.; Liu, N.; Zhang, M.; Wang, D. Oxidative desulfurization of dibenzothiophene over monoclinic VO₂ phase-transition catalysts. *Appl. Catal., B* **2017**, *212*, 32–40.
- (19) Zhang, G.; Liu, B.; Zhou, H.; Yang, Y.; Chen, W.; Zhao, J. Graphene wrapped phthalocyanine: Enhanced oxidative desulfurization for dibenzothiophene in fuel. *Appl. Organomet. Chem.* **2018**, *32*, 1–8.
- (20) Lu, L.; He, J.; Wu, P.; Wu, Y.; Chao, Y.; Li, H.; Tao, D.; Fan, L.; Li, H.; Zhu, W. Taming electronic properties of boron nitride nanosheets as metal-free catalysts for aerobic oxidative desulfurization of fuels. *Green Chem.* **2018**, *20*, 4453–4460.
- (21) Bhasarkar, J. B.; Dikshit, P. K.; Moholkar, V. S. Ultrasound assisted biodesulfurization of liquid fuel using free and immobilized cells of *Rhodococcus rhodochrous* MTCC 3552: A mechanistic investigation. *Bioresour. Technol.* **2015**, *187*, 369–378.
- (22) Jha, D.; Haider, M. B.; Kumar, R.; Balathanigaimani, M. S. Extractive desulfurization of dibenzothiophene using phosphonium-based ionic liquid: Modeling of batch extraction experimental data and simulation of continuous extraction process. *Chem. Eng. Res. Des.* **2016**, *111*, 218–222.
- (23) Li, F. T.; Liu, Y.; Sun, Z. M.; Chen, L. J.; Zhao, D. S.; Liu, R. H.; Kou, C. G. Deep extractive desulfurization of gasoline with xEt₃NHCl-FeCl₃ ionic liquids. *Energy Fuels* **2010**, *24*, 4285–4289.
- (24) Ko, N. H.; Lee, J. S.; Huh, E. S.; Lee, H.; Jung, K. D.; Kim, H. S.; Cheong, M. Extractive desulfurization using Fe-containing ionic liquids. *Energy Fuels* **2008**, *22*, 1687–1690.
- (25) Kuhlmann, E.; Haumann, M.; Jess, A.; Seeberger, A.; Wasserscheid, P. Ionic liquids in refinery desulfurization: Comparison between biphasic and supported ionic liquid phase suspension processes. *ChemSusChem* **2009**, *2*, 969–977.
- (26) Xiong, J.; Zhu, W.; Li, H.; Ding, W.; Chao, Y.; Wu, P.; Xun, S.; Zhang, M.; Li, H. Few-layered graphene-like boron nitride induced a remarkable adsorption capacity for dibenzothiophene in fuels. *Green Chem.* **2015**, *17*, 1647–1656.
- (27) Sarda, K. K.; Bhandari, A.; Pant, K. K.; Jain, S. Deep desulfurization of diesel fuel by selective adsorption over Ni/Al₂O₃ and Ni/ZSM-5 extrudates. *Fuel* **2012**, *93*, 86–91.
- (28) Xiong, J.; Yang, L.; Chao, Y.; Pang, J.; Zhang, M.; Zhu, W.; Li, H. Boron Nitride Mesoporous Nanowires with Doped Oxygen Atoms for the Remarkable Adsorption Desulfurization Performance from Fuels. *ACS Sustainable Chem. Eng.* **2016**, *4*, 4457–4464.
- (29) Seredych, M.; Khine, M.; Bandoz, T. J. Enhancement in dibenzothiophene reactive adsorption from liquid fuel via incorporation of sulfur heteroatoms into the nanoporous carbon matrix. *ChemSusChem* **2011**, *4*, 139–147.
- (30) Hernández-Maldonado, A. J.; Yang, F. H.; Qi, G.; Yang, R. T. Desulfurization of transportation fuels by π -complexation sorbents: Cu(I)-, Ni(II)-, and Zn(II)-zeolites. *Appl. Catal., B* **2005**, *56*, 111–126.
- (31) Xue, M.; Chitrakar, R.; Sakane, K.; Hirotsu, T.; Ooi, K.; Yoshimura, Y.; Toba, M.; Feng, Q. Preparation of cerium-loaded Y-zeolites for removal of organic sulfur compounds from hydrodesulfurized gasoline and diesel oil. *J. Colloid Interface Sci.* **2006**, *298*, 535–542.
- (32) Kwon, J.-M.; Moon, J.-H.; Bae, Y.-S.; Lee, D.-G.; Sohn, H.-C.; Lee, C.-H. Adsorptive Desulfurization and Denitrogenation of Refinery Fuels Using Mesoporous Silica Adsorbents. *ChemSusChem* **2008**, *1*, 307–309.
- (33) Wang, Y.; Yang, R. T. Desulfurization of liquid fuels by adsorption on carbon-based sorbents and ultrasound-assisted sorbent regeneration. *Langmuir* **2007**, *23*, 3825–3831.
- (34) Krishnakumar, T.; Pinna, N.; Kumari, K. P.; Perumal, K.; Jayaprakash, R. Microwave-assisted synthesis and characterization of tin oxide nanoparticles. *Mater. Lett.* **2008**, *62*, 3437–3440.
- (35) Li, G. J.; Zhang, X. H.; Kawi, S. Relationships between sensitivity, catalytic activity, and surface areas of SnO₂ gas sensors. *Sens. Actuators, B* **1999**, *60*, 64–70.
- (36) Seza, A.; Soleimani, F.; Naseri, N.; Soltaninejad, M.; Montazeri, S. M.; Sadrezaad, S. K.; Mohammadi, M. R.; Moghadam, H. A.; Forouzandeh, M.; Amin, M. H. Novel microwave-assisted synthesis of porous g-C₃N₄/SnO₂ nanocomposite for solar water-splitting. *Appl. Surf. Sci.* **2018**, *440*, 153–161.
- (37) Yan, S. C.; Li, Z. S.; Zou, Z. G. Photodegradation performance of g-C₃N₄ fabricated by directly heating melamine. *Langmuir* **2009**, *25*, 10397–10401.
- (38) He, Y.; Zhang, L.; Fan, M.; Wang, X.; Walbridge, M. L.; Nong, Q.; Wu, Y.; Zhao, L. Z-scheme SnO₂/g-C₃N₄ composite as an efficient photocatalyst for dye degradation and photocatalytic CO₂ reduction. *Sol. Energy Mater. Sol. Cells* **2015**, *137*, 175–184.
- (39) Lin, H.; Huang, C. P.; Li, W.; Ni, C.; Shah, S. I.; Tseng, Y. H. Size dependency of nanocrystalline TiO₂ on its optical property and photocatalytic reactivity exemplified by 2-chlorophenol. *Appl. Catal., B* **2006**, *68*, 1–11.
- (40) Cao, J.; Qin, C.; Wang, Y.; Zhang, B.; Gong, Y.; Zhang, H.; Sun, G.; Bala, H.; Zhang, Z. Calcination Method Synthesis of SnO₂/g-C₃N₄ Composites for a High-Performance Ethanol Gas Sensing Application. *Nanomaterials* **2017**, *7*, 98.
- (41) Mahdi, L. M.; Rezaee, R.; Saeedi, A.; Al Hinai, A. Journal of Petroleum Science and Engineering Evaluation of pore size spectrum of gas shale reservoirs using low pressure nitrogen adsorption, gas expansion and mercury porosimetry: A case study from the Perth and Canning Basins, Western Australia. *J. Pet. Sci. Eng.* **2013**, *112*, 7–16.
- (42) Dehghani, M. H.; Taher, M. M.; Bajpai, A. K.; Heibati, B.; Tyagi, I.; Asif, M.; Agarwal, S.; Gupta, V. K. Removal of noxious Cr(VI) ions using single-walled carbon nanotubes and multi-walled carbon nanotubes. *Chem. Eng. J.* **2015**, *279*, 344–352.
- (43) Salehi, E.; Afshar, S.; Mehrizi, M. Z.; Chehrei, A.; Asadi, M. Direct reduction of blood serum cholesterol using *Thymus vulgaris* L: Preliminary biosorption study. *Process Biochem.* **2018**, *67*, 155–164.
- (44) Polanyi, M. Section III.—Theories of the adsorption of gases. A general survey and some additional remarks. Introductory paper to section III. *Trans. Faraday Soc.* **1932**, *28*, 316–333.

- (45) Jain, M.; Garg, V. K.; Kadirvelu, K. Chromium(VI) removal from aqueous system using *Helianthus annuus* (sunflower) stem waste. *J. Hazard. Mater.* **2009**, *162*, 365–372.
- (46) Heibati, B.; Rodriguez-Couto, S.; Amrane, A.; Rafatullah, M.; Hawari, A.; Al-Ghouti, M. A. Uptake of Reactive Black 5 by pumice and walnut activated carbon: Chemistry and adsorption mechanisms. *J. Ind. Eng. Chem.* **2014**, *20*, 2939–2947.
- (47) Kim, J. H.; Ma, X.; Zhou, A.; Song, C. Ultra-deep desulfurization and denitrogenation of diesel fuel by selective adsorption over three different adsorbents: A study on adsorptive selectivity and mechanism. *Catal. Today* **2006**, *111*, 74–83.
- (48) Ren, X.; Liu, Z.; Dong, L.; Miao, G.; Liao, N.; Li, Z.; Xiao, J. Dynamic catalytic adsorptive desulfurization of real diesel over ultra-stable and low-cost silica gel-supported TiO₂. *AIChE J.* **2018**, *64*, 2146–2159.
- (49) Ma, X.; Velu, S.; Kim, J. H.; Song, C. Deep desulfurization of gasoline by selective adsorption over solid adsorbents and impact of analytical methods on ppm-level sulfur quantification for fuel cell applications. *Appl. Catal., B* **2005**, *56*, 137–147.
- (50) Vattikuti, S. V. P.; Reddy, P. A. K.; Shim, J.; Byon, C. Visible-Light-Driven Photocatalytic Activity of SnO₂–ZnO Quantum Dots Anchored on g-C₃N₄ Nanosheets for Photocatalytic Pollutant Degradation and H₂ Production. *ACS Omega* **2018**, *3*, 7587–7602.
- (51) Duan, F.; Chen, C.; Wang, G.; Yang, Y.; Liu, X.; Qin, Y. Efficient adsorptive removal of dibenzothiophene by graphene oxide-based surface molecularly imprinted polymer. *RSC Adv.* **2014**, *4*, 1469–1475.
- (52) Saleh, T. A.; Sulaiman, K. O.; Al-hammadi, S. A.; Dafalla, H.; Danmaliki, G. I. Adsorptive desulfurization of thiophene, benzothiophene and dibenzothiophene over activated carbon manganese oxide nanocomposite: with column system evaluation. *J. Cleaner Prod.* **2017**, *154*, 401–412.
- (53) Sadrnezhaad, A. N. S. K.; Gharavi, A. Software for Kinetic Process Simulation, 2003 <http://www.ije.ir/Vol16/No1/A/7-28.pdf>.
- (54) Malik, U. R.; Hasany, S. M.; Subhani, M. S. Sorptive potential of sunflower stem for Cr(III) ions from aqueous solutions and its kinetic and thermodynamic profile. *Talanta* **2005**, *66*, 166–173.
- (55) Wang, S.; Li, P.; Zhang, X.; Zheng, S.; Zhang, Y. Selective adsorption of lithium from high Mg-containing brines using H_xTiO₃ ion sieve. *Hydrometallurgy* **2017**, *174*, 21–28.